Oxidative Dehydrogenation of Ethane over Boron-Containing Chabazite

Mi Jen Kuo[†], Xinlei Huang[†], Sunkyu Kim[†], Nicholas Houck[†], Shi Bai[‡], Dionisios G. Vlachos[†], and Raul F. Lobo[,†]*

[†] Center for Catalytic Science and Technology, Department of Chemical and Biomolecular Engineering, University of Delaware, Newark, Delaware 19716, United States

[‡] Department of Chemistry and Biochemistry, University of Delaware, Newark, Delaware 19716, United States

KEYWORDS

Oxidative dehydrogenation; ethylene; boron; mechanism; zeolite

ABSTRACT

We report that boron-containing zeolite chabazite (B-CHA) catalyzes the oxidative dehydrogenation of ethane (ODHE) with high selectivity (>70%) and excellent stability in the temperature range of 500-600 °C. ODHE rates, in fact, increase over time-on-stream. Ethane consumption rate ($-r_{C2H6}$) has an apparent activation energy (E_{app}) of 125 kJ mol^{-1}, with Langmuirian dependence on the oxygen partial pressure (p_{O2}) and first-order dependence on the ethane partial pressure (p_{C2H6}). Investigation of the catalyst before and after reaction by one-dimensional ^{11}B magic angle spinning (1D ^{11}B MAS) nuclear magnetic resonance (NMR), two-dimensional ^{11}B multiple quantum MAS (2D ^{11}B MQMAS) NMR spectroscopy, and Fourier transform infrared (FTIR) spectroscopy identifies the B-OH group in defect trigonal boron ($B(OSi)(OH)_2$) as the species initiating the ODHE reaction. This result could open a pathway to develop suitable catalysts for industrial ethylene production with lower greenhouse gas emissions than current non-oxidative dehydrogenation routes.

▪ Introduction

Ethylene is the largest organic intermediate in the chemical industry with a global production capacity of 214 million metric tons in 2021.[1–4] Ethylene production is also the second largest source of greenhouse gas emissions in the chemical industry, producing over 1 ton of CO_2-equivalent emissions per ton of ethylene.[5] This stems from the fact that ethylene production uses non-oxidative and non-catalytic processes—such as ethane steam cracking—which require a high reaction temperature (>1073 K) to overcome the thermodynamic limitations of this highly endothermic reaction.[6–10] The expanding global demand for ethylene further drives interest in developing novel catalytic routes to ethylene production,[2,6] and the oxidative dehydrogenation of ethane (ODHE) is an attractive alternative due to its low energy demand and the *in-situ* carbon-deposits removal by the oxygen present in the feed.[2] However, the poor selectivity caused by the overoxidation of reactants and products into carbon oxides is a barrier that has yet to be overcome, and new catalysts for selective ODHE remain urgently needed.[11]

Both reducible and non-reducible metal oxides have been widely investigated for ODHE.[2,11,12] Morales and Lunsford reported that Li^+/MgO catalysts achieve 75% ethylene selectivity at 40% ethane conversion at 600 °C in 1989.[13] A wide variety of vanadium and nickel oxides mixed with Mo, Nb, Mg, and Ce also catalyze the ODHE.[2] Linde and Clariant have developed ODHE process with M1 catalyst, resulting in a combined selectivity (ethylene and acetic acid) of 93%;[10,14–16] this process has been demonstrated at a commercial scale. On the other hand, boron-containing heterogeneous catalysts, such as hexagonal boron nitride (*h*-BN), metal borides, and supported boron oxides, catalyze the oxidative dehydrogenation of *propane* (ODHP) to propene with excellent selectivity. Grant et al. first reported the ODHP using the *h*-BN catalyst with 79% propene selectivity at 14% propane conversion.[17] Zhou et al. reported a boron-containing MFI-

type zeolite catalyst with 55% propene selectivity and 26% ethylene selectivity at 41% propane conversion.[18] *h*-BN has also been utilized in ODHE:[2,19–25] Zhou et al. reported 79% and 68% ethylene selectivity at 36% and 44% ethane conversions over activated *h*-BN at 575 and 590 °C,[21] and Wu et al. presented 80% ethylene selectivity at 20% ethane conversion over commercial *h*-BN at 600 °C.[25]

h-BN catalyzes ODHP through an Eley-Rideal mechanism that combines surface and gas-phase reaction networks including surface initiation and free-radical gas-phase propagation; the reaction kinetics have Langmuir adsorption dependence on p_{O2} and second-order dependence on p_{C3H8},[17,26–29] a universal feature of the *h*-BN catalyst.[12,28,30] The second-order dependence on p_{C3H8} suggests that propane reacts directly from the gas phase with active oxygen species, in agreement with a mixed surface-gas mechanism.[27–29,31] The borosilicate catalyst with the MFI zeolite framework also shows Langmuir adsorption dependence on p_{O2} but first-order dependence on p_{C3H8} in ODHP.[18] To explain this difference in catalytic kinetics, Zhou et al proposed a propane-oxygen co-activation mechanism in which the reaction pathways occur at the surface without gas-phase involvement.[18] Tian et al. investigated the influence of spatial confinement on the kinetics of boron oxide supported on mesoporous silicas with different pore diameters, revealing that the propane reaction order could vary from 1 to 3 depending on the pore size of the support, B_2O_3 loading, and p_{C3H8}.[30]

Grant et al. first proposed that an oxygen-terminated armchair edge of BN (>B-O-O-N<) works as the active site for the ODHP reaction.[17] Venegas et al. further suggested that BO• species formed by the cleavage of >B-O-O-B< can react with oxygen to form the free radical HOO• over *h*-BN, leading to the mixed surface and gas-phase propane H abstraction.[28] Tian et al proposed that the reaction between boron and oxygen forms the boron peroxyl radical (BOO•), which initiates gas-

phase propagation in *h*-BN-catalyzed ODHP.[27] On the other hand, Zhou et al. reported a novel isolated active site of -B[OH…O(H)-Si]$_2$ in the MFI zeolite framework, showing exceptional olefin selectivity in ODHP without gas-phase chemistry, which is very different from the *h*-BN catalyst mechanism.[18]

Chabazite-type (CHA) catalysts are used commercially in the methanol-to-olefins process and the selective catalytic reduction of NO_x with ammonia.[32,33] The most salient feature of CHA zeolite is that it is formed by cages accessed only through 8-ring windows of ~3.9Å in diameter (Figure 1). This is sufficiently large to allow the facile diffusion of ethane, ethylene, and smaller molecules, but propane diffusion in CHA is slower than ethane by a factor of over 10^4, with D_{C2}/D_{C3}~ $3.7 \cdot 10^6$ and $5.6 \cdot 10^4$ at 30 °C and 80 °C respectively.[34] There are six 8-ring windows per cage and the cage is formed by 36 T-atoms (T=$TO_{4/2}$, where T is Si or B) and is ~7.4Å in diameter. CHA is structurally simple because the crystallographic asymmetric unit contains only one $SiO_{4/2}$ tetrahedron while MFI has twelve, simplifying the interpretation of CHA zeolite spectroscopic results. CHA also has a large microporous volume (~0.30 $cm^3\ g^{-1}$), a high surface area (~300 $m^2\ g^{-1}$), and abundant Si-OH group defects. Heats of adsorption of ethane and ethylene in siliceous CHA are low and dominated by van der Waals forces (28.9 kJ mol^{-1} and 27.2 kJ mol^{-1} respectively).[34]

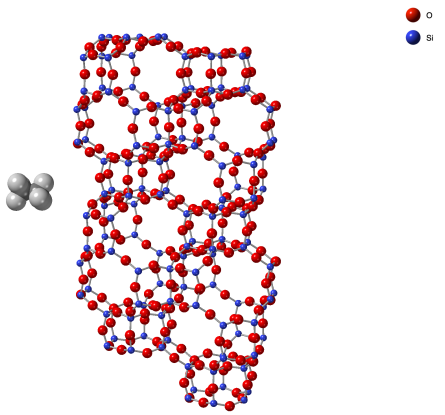

Figure 1. Illustration of zeolite chabazite (CHA) crystal structure. Apical O atoms are depicted in red and framework T-atoms (Si, B) in blue. A molecule of ethane is depicted to scale to compare the dimensions of the pore windows and cages to the molecule's.

Here, we report a boron-chabazite zeolite (B-CHA) showing excellent ODHE reaction rates, with high selectivity towards ethylene from 500-600 °C. Catalytic rates of ODHE, in fact, increase over time-on-stream; this suggests that partial framework deboronation of B-CHA increases the number of active sites.[35] The negligible decrease of boron content in the spent B-CHA catalyst also suggests that a barrier to diffusion of boron species caused by the zeolite small pores enhances catalyst stability.[18] The dependence of $-r_{C2H6}$ on p_{C2H6} and p_{O2} changes with temperature (560-600 °C), consistent with a change of ethane activation pathways. Solids-state ^{11}B MAS NMR and FTIR spectroscopy investigations show that catalytic rates increase as the number of B-OH groups in the catalyst grows, a result consistent with the structural characterizations and the catalyst stability test. On the other hand, the high concentration of Si-OH groups facilitates the distribution of boron species on the high surface area, leading to high ODHE activity.

- **Experimental Methods**

Materials. Boric acid ($B(OH)_3$) and tetraethylorthosilicate (TEOS, 98 wt%) were obtained from Sigma-Aldrich. Trimethyladamantylammonium hydroxide solution (TMAdaOH, 25 wt%) and tetrapropylammonium hydroxide solution (TPAOH, 40 wt%) were purchased from Sachem Inc (aqueous technical grade). Carbosil M5 fumed silica was supplied by Cabot Inc. Hexagonal boron nitride (*h*-BN, 99.5% (metal basis), product number: 11078) was supplied by Fisher Scientific. Hydrofluoric acid (HF, 48–51%) was supplied by Acros Organics. Ethane, oxygen, and helium gases (>99%) were supplied by Keen Compressed Gas Co. These raw materials were used as received without further treatment.

Material Synthesis.

Synthesis of the B-CHA catalyst. The boron-containing CHA zeolite was synthesized according to previously reported procedures.[36] First, a 17.2 g trimethyladamantylammonium hydroxide solution (TMAdaOH, 25 wt%) was added to 20.7 g deionized (DI) water. After that, 0.413 g boric acid ($B(OH)_3$) was dissolved in the solution with stirring for 30 min. Finally, 5.03 g Carbosil M-5 was added to the resulting solution while being stirred. The mixture was stirred for another 30 min to afford a slightly viscous gel. The gel was transferred to a 45 mL Teflon-lined autoclave and heated at 160 °C for 3 days under rotation. After the crystallization, the autoclave was cooled down and then opened. The zeolite product was washed with 20 mL DI water and centrifuged at 4500 rpm for 20 min, which was repeated 5 times then dried at 80 °C overnight. The as-made zeolite was placed in the tube furnace inside a rectangular crucible and calcined at 580 °C in flowing air for 8 h with a ramping rate of 2 °C min^{-1} to remove the organic structure-directing agent (SDA). The powder product after calcination is denoted as B-CHA. Note that there is no sodium or other

inorganic cations in the zeolite synthesis and thus B-framework sites are expected to be balanced by protons. The only inorganic species in the synthesis gel are silica and boric acid.

Synthesis of the Si-CHA catalyst. The pure-silica (siliceous) CHA zeolite was synthesized according to previously reported procedures.[37,38] First, a solution of 11.78 g tetraethylorthosilicate (TEOS, 98 wt%) and 23.87 g trimethyladamantylammonium hydroxide solution (TMAdaOH, 25 wt%) was stirred for 24 h at room temperature. With continuous stirring, the solution was heated to evaporate 13.4 g water and 10.4 g ethanol (23.8 g total), resulting in a final H_2O/SiO_2 ratio of 3. Finally, 1.18 g hydrofluoric acid (HF, 48–51%) was added. The thick paste was transferred to a 23 mL Teflon-lined autoclave and heated at 150 °C for 2 days under rotation. After the crystallization, the autoclave was cooled down and then opened. The zeolite product was washed with DI water and recovered by filtration, then dried at 80 °C overnight. The as-made zeolite was calcined at 550 °C in flowing air for 8 h with a ramping rate of 3 °C min^{-1}. The powder product after calcination is denoted as Si-CHA.

Synthesis of the B-MFI catalyst. The boron-containing MFI zeolite was synthesized according to previously reported procedures.[18] First, 0.09 g boric acid and 6 g Carbosil M-5 were mixed in a mortar. After that, 4.8 g tetrapropylammonium hydroxide solution (TPAOH, 40 wt%) was added to the mixture and ground for 30 min. The powder mixture was transferred to a 45 mL Teflon-lined autoclave and heated at 180 °C for 3 days. After the crystallization, the autoclave was cooled down and then opened. The zeolite product was washed with DI water and recovered by centrifugation, then dried at 80 °C overnight. The as-made zeolite was calcined at 550 °C in flowing air for 8 h with a ramping rate of 5 °C min^{-1}. The powder product after calcination is denoted as B-MFI.

Characterization. Powder X-ray diffraction (XRD) patterns were obtained using a Bruker powder diffractometer (D8 XRD) with a Cu Kα radiation (40 kV, 40 mA) as the X-ray source, in the range 2θ = 4-50° for zeolite samples and 10-80° for *h*-BN samples with a step size of 0.04° and 1 s per step. The catalyst samples' morphology and elemental mapping were determined using a scanning electron microscope (SEM, Auriga-60, ZEISS) and energy-dispersive X-ray spectroscopy (EDS) spectra respectively. Prior to the SEM measurement, the samples were coated with gold/palladium alloy. Textural properties of all catalysts were obtained by employing N_2 physisorption experiments at 77 K on a 3Flex surface characterization analyzer (Micromeritics). Before the physisorption experiments, all the samples were degassed at 300 °C overnight under vacuum. The micropore volume was determined using the *t*-plot method and the specific surface area was determined using the BET method.[39,40] The boron and silica contents of the calcined zeolite samples were determined by inductively coupled plasma optical emission spectrometry (ICP-OES) analysis (Galbraith Laboratories, TN). All the NMR measurements were performed on a Bruker AVANCE-III 500 MHz spectrometer operating at the resonance frequency of 160.46 MHz and 99.347 MHz for the ^{11}B and ^{29}Si nucleus respectively, with a Bruker 4.0 mm multinuclear HX MAS probe at a spinning rate of 10 kHz within ± 3 Hz. A broad background boron signal from the MAS stator materials was removed using a DEPTH pulse sequence with a small tippling angle θ corresponding to a rf pulse length of 1.9 μs.[41] The effectiveness of boron background removal was verified by a rotor packed with glycine. A 3-pulse (5.7 μs, 1.9 μs, and 20 μs) pulse program with a z-filter was used to acquire 2D MQMAS spectra.[42] The number of scans was set to 900 with 64 increments in evolution dimension. A 2D MQMAS spectra were processed by first applying Fourier transform to both dimensions followed by a shearing transformation. A 2-s recycle delay was used for all ^{11}B experiments and all ^{11}B NMR spectra were referenced to a sharp resonance of

$NaBH_4$ at -42.01 ppm as a secondary external reference.[43] Fourier transform infrared (FTIR) spectra were collected on an Agilent CARY 660 spectrometer equipped with an MCT detector.[39] First, the sample (~50 mg) was pressed into a thin disk and placed in the cell quipped with KBr windows. The samples were heated to 550 °C for 1 h under vacuum for dehydration to remove adsorbed molecules and cooled down to each measurement temperature. The spectra were collected by averaging 32 scans with a resolution of 4 cm^{-1} against the background spectrum taken with an empty cell. X-ray photoelectron spectroscopy (XPS) spectra were collected using a Thermo Fisher K-Alpha+ system. Thermogravimetric analysis (TGA) was conducted on Discovery TGA instrument under an airflow of 50 mL min^{-1}, with a temperature ramping from room temperature to 700 °C at a rate of 5 °C min^{-1}.

Catalytic Reactions and Kinetic Measurements.

Catalytic reaction in a fixed-bed flow reactor. The catalyst samples in powder form were pressed, crushed, and sieved (20-40 mesh) to particle sizes ranging from 400 to 841 μm. The ODHE was measured in a fixed-bed quartz reactor (I.D. = 4 mm, O.D. = 6 mm, length = 536 mm). The catalyst bed was kept in place using silica glasswool plugs. A thermocouple was placed adjacent to the catalyst bed for temperature control and measurement. In each experiment, the reactor was first heated to the highest temperature (typically 600 °C) with a ramping rate of 5 °C min^{-1} under 20 vol% O_2/ 80 vol% He (total flow rate = 15 mL min^{-1}). After the temperature stabilized, the catalysts were treated with the reaction mixture with a composition of 20 vol% C_2H_6/ 12 vol% O_2/ 68 vol% He (total flow rate = 15 mL min^{-1}) until stable conversion was obtained as there is an activity induction period for boron-containing catalysts.[26,27,44] For the temperature-dependent experiments, the temperature was then reduced to the desired temperature, and the reaction was run for predetermined time intervals. The average results over the interval were used to compute the

results. The catalyst samples after the temperature-dependent experiments were used for ~20 h and are denoted as the catalysts after 20 h ODHE. The reactor effluent was injected into an online gas chromatograph (GC) (Agilent 7890) equipped with a flame ionization detector (FID) and a thermal conductivity detector (TCD) after going through a condenser. The FID with an RT-Q-BOND column was used for CH_4 analysis. The TCD had a HayeSep Q column and a Molseive 13X column in a series configuration and was used for C_2H_6, O_2, C_2H_4, CO, and CO_2 analysis. Ethane and oxygen conversions (X_{C2H6}, X_{O2}), product selectivity (S_i), carbon balance (C.B.), the ethane consumption rate $-R_{C2H6}$ ($mmol_{C2H6}$ mol_B^{-1} h^{-1}) and $-r_{C2H6}$ ($mmol_{C2H6}$ g_{cat}^{-1} h^{-1}), and product formation rates (R_i and r_i) were calculated as follows:[18,26,39]

$$\text{C. B.} = \frac{2 \times F_{\text{C2H6,out}} + \Sigma\, n_i \times F_{i,\text{out}}}{2 \times F_{\text{C2H6,in}}} \times 100\%$$

$$S_i = \frac{n_i \times F_{i,\text{out}}}{\Sigma\, n_i \times F_{i,\text{out}}} \times 100\%$$

$$X_{\text{C2H6}} = \frac{F_{\text{C2H4,out}}/S_{\text{C2H4}}}{F_{\text{C2H6,in}}} \times 100\%$$

$$X_{\text{O2}} = \frac{F_{\text{O2,in}} - F_{\text{O2,out}}}{F_{\text{O2,in}}} \times 100\%$$

$$-R_{\text{C2H6}} = \frac{F_{\text{C2H6,in}} \times X_{\text{C2H6}} \times M_{\text{boron}}}{m_{\text{cat}} \times I_{\text{boron}}}$$

$$R_i = (-R_{\text{C2H6}}) \times S_i$$

$$-r_{\text{C2H6}} = \frac{F_{\text{C2H6,in}} \times X_{\text{C2H6}}}{m_{\text{cat}}}$$

$$r_i = (-r_{\text{C2H6}}) \times S_i$$

Where $F_{C2H6,in}$ and $F_{C2H6,out}$ represent the molar flow rate of C_2H_6 at the inlet and outlet of the reactor, $F_{O2,in}$ and $F_{O2,out}$ represent the molar flow rate of O_2 at the inlet and outlet of the reactor, i represents the ODHE products C_2H_4, CO, CO_2, CH_4 in the effluent gas, n_i is the number of carbon atoms of component i, $F_{i,out}$ is the molar flow rate of product i at the outlet of the reactor, M_{boron} is the molar mass of atom boron, I_{boron} (%) is the boron weight content in the catalyst and m_{cat} (g) is the catalyst weight used in the experiment. C.B.s were above 90% in all but one experiment (86% at 43% conversion and 600 °C). Acetic acid was considered an insignificant byproduct with high C.B.s. By carrying out experiments in the temperature range (500-600 °C) with an empty tube and a tube filled with quartz sand, the potential for gas-phase initiated reactions is excluded with negligible ethane conversions in all these experiments.[45] The rate was measured at differential conversion (<12%) for kinetic investigations. The activation energy, E_{app} , was determined in the temperature range of 500-600 °C. Catalysts were then continuously used for p_{C2H6} and p_{O2} experiments. The dependences of the rate $-r_{C2H6}$ on p_{C2H6} and p_{O2} were determined at 560, 580, and 600 °C by changing the ethane flow rate (1-3.6 mL min^{-1}) and oxygen flow rate (0-3 mL min^{-1}), with a total flow rate of 15 mL min^{-1} at STP. The rates obtained in p_{C2H6} and p_{O2} experiments were normalized by the initial rates obtained in the E_{app} experiments (with the same conditions) to account for any changes in catalyst activity. For the stability test, data points were collected for ~60 h at the desired temperature after the activity stabilized, and 21 data points shown were selected from the GC traces with similar time intervals but not exactly 3 h. The catalyst samples after the stability tests were used for ~60 h and are denoted as catalysts after 60 h ODHE. For the B-CHA catalyzed reactions, B-CHA (20 h ODHE) went through the temperature-dependent experiments while B-CHA (60 h ODHE) went through the temperature-dependent experiments but ran for ~60 h at 580 °C for the stability test. Results from these two runs of experiments were

used in Figure 2C: for 500-560 °C, the results of the second run were used due to higher conversion; for 580 °C, the average results of these two runs (initial conversions of the second run) were used; for 600 °C, the average results of these two runs were used. For the B-MFI catalyzed reactions, there were small CO and CO_2 peaks even when the conversion was zero at a low temperature of around 400 °C (probably due to remaining SDA), and were therefore deducted when analyzing B-MFI results. Also, the temperature range for B-MFI experiments was elevated to 520-620 °C due to low activity at 500-600 °C.

- **Results**

Structure and Properties of the As-prepared Catalysts. According to the EDS analysis, the *h*-BN catalyst had a boron content of 44.9 wt%, while ICP analysis showed that B-CHA and B-MFI had boron contents of 1.01 and 0.31 wt% respectively (Table S1). The three catalysts were characterized by XRD, SEM, N_2 physisorption isotherms, and XPS analysis (Figures S1-S13). B-CHA and B-MFI diffraction patterns were indexed to the corresponding diffraction peaks of CHA and MFI, confirming the structure and the absence of any crystalline impurities (Figures S5 and S10).[26,46] Figures S6A and S11A show SEM images of B-CHA and B-MFI, revealing average crystal sizes of 3.9 μm and 365 nm respectively (Figures S6D and S11C). B-CHA showed a pseudo-cubic crystal morphology while B-MFI was composed of crystalline spheroidal particles with a roughed external surface. The N_2 physisorption results showed a type-I isotherm for B-CHA (Figure S7), and a larger micropore volume (0.26 $cm^3\ g^{-1}$) and BET surface area (538 $m^2\ g^{-1}$) than B-MFI (0.13 $cm^3\ g^{-1}$, 346 $m^2\ g^{-1}$) (Table S1) as expected from the structure of these zeolites.

Catalytic Properties of the B-samples. Figure 2A plots the ethylene selectivity versus the ethane conversion, with the boron-containing catalysts having better ethylene selectivity than most of the reported vanadium and nickel-containing catalysts. *h*-BN afforded high ethylene selectivity at different conversions as reported in references,[19–25] with 95% and 75% ethylene selectivity at 11% and 43% ethane conversions respectively. B-CHA also displayed excellent ethylene selectivity, with 87% and 72% ethylene selectivity at 22% and 43% ethane conversions respectively. B-MFI, however, did not achieve as high ethylene selectivity, with 75% and 72% ethylene selectivity at 11% and 22% ethane conversions respectively. The selectivity of these three boron catalysts is compared in Figure 2B at similar conversions and the same reaction temperatures. High ethylene

selectivity was obtained over B-CHA, with CO and CO_2 as the main byproducts (X_{C2H6} = 14%, S_{C2H4} = 87%, S_{CO} = 8%, S_{CO2} = 3%, S_{CH4} = 2%). In the *h*-BN catalyzed reactions, ethylene was also the dominant product, with CO as the major byproduct, and no CO_2 was observed (X_{C2H6} = 14%, S_{C2H4} = 94%, S_{CO} = 4%, S_{CO2} = 0%, S_{CH4} = 2%). However, B-MFI, a zeolite-based catalyst widely used for ODHP,[18,26] showed modest ethylene selectivity with a large amount of CO_2 produced (X_{C2H6} = 12%, S_{C2H4} = 61%, S_{CO} = 14%, S_{CO2} = 24%, S_{CH4} = 1%).

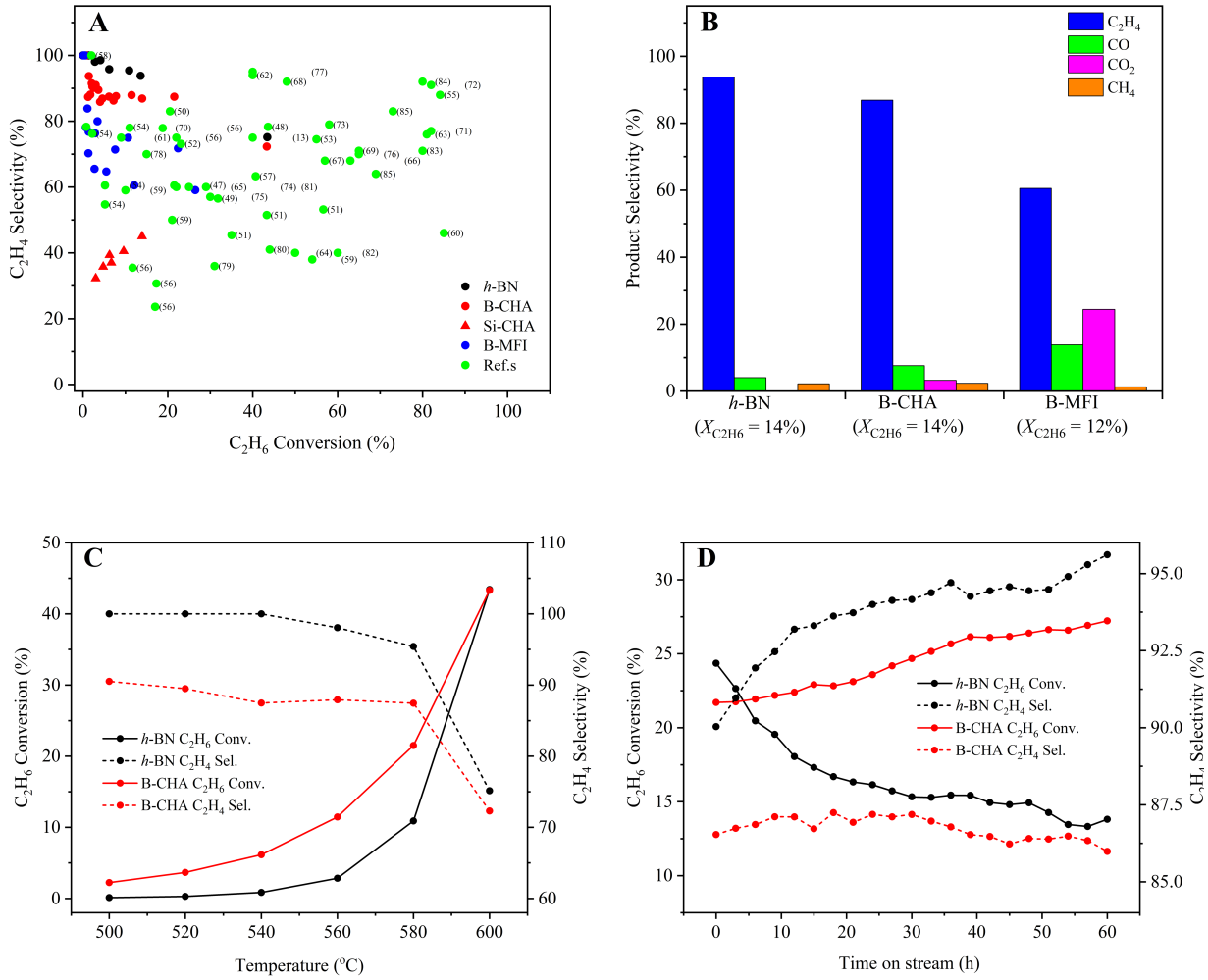

Figure 2. (**A**) Ethylene selectivity plotted against ethane conversion for ODHE over the *h*-BN, B-CHA, and B-MFI catalysts. Reaction conditions: catalyst 125-750 mg, 500-600 °C for *h*-BN and B-CHA, 520-620 °C for B-MFI, gas feed 15 mL min^{-1}, 20 vol% C_2H_6, 12 vol% O_2, He balance, 0.1 MPa. Catalyst amounts and reaction temperatures were adjusted to obtain different conversions. The green circles represent reported data, with the number indicating the reference number and the reaction conditions being summarized in Table S2.[13,47–85] (**B**) Comparisons of the product selectivity between the *h*-BN (250 mg), B-CHA (250 mg), and B-MFI (750 mg) catalysts. Reaction conditions: 600 °C, gas feed 15 mL min^{-1}, 20 vol% C_2H_6, 12 vol% O_2, He balance, 0.1 MPa. Ethane conversion and ethylene selectivity plotted against (**C**) reaction temperature and (**D**) time-on-stream for ODHE over the *h*-BN and B-CHA catalysts. Reaction conditions of (**C**): catalyst 750 mg, 500-600 °C, gas feed 15 mL min^{-1}, 20 vol% C_2H_6, 12 vol% O_2, He balance, 0.1 MPa. Reaction conditions of (**D**): catalyst 750 mg, 590 °C for the *h*-BN catalyst and 580 °C for the B-CHA catalyst, gas feed 15 mL min^{-1}, 20 vol% C_2H_6, 12 vol% O_2, He balance, 0.1 MPa.

B-CHA achieved 22 and 43% ethane conversions at 580 and 600 °C respectively (Figure 2C), with ethane consumption rates $-R_{C2H6}$ of 24.9 and 50.1 $mmol_{C2H6}$ mol_B^{-1} h^{-1}. Meanwhile, *h*-BN exhibited 11 and 43% ethane conversions at 580 and 600 °C, with $-R_{C2H6}$ of 0.284 and 1.13 $mmol_{C2H6}$ mol_B^{-1} h^{-1}. B-CHA exhibited higher $-R_{C2H6}$ than *h*-BN, possibly due to the higher micropore volume and surface area (higher B sites availability). Both *h*-BN and B-CHA maintained high ethylene selectivity in the reaction temperature from 500-600 °C. Moreover, the similar product distribution for B-CHA and *h*-BN may suggest a similar underlying reaction mechanism for these two boron-containing catalysts (Figures S14 and S15).

The stability and structural integrity of *h*-BN and B-CHA after ODHE were analyzed using several techniques (Figure 2D). The ODHE catalytic activity at 590 °C of *h*-BN decreased over time (t ~ 0, X_{C2H6} = 24%, S_{C2H4} = 90%; t ~ 60 h, X_{C2H6} = 14%, S_{C2H4} = 96%) (Figure S16), as has been found by others.[18] The poor stability of *h*-BN could be attributed to the formation of boric acid during ODHE (Figure S1). In contrast, B-CHA showed a small but monotonic increase in conversion as a function of time-on-stream: B-CHA achieved a higher final conversion than initially while maintaining high ethylene selectivity after 60 h ODHE at 580 °C (t ~ 0, X_{C2H6} = 22%, S_{C2H4} = 87%; t ~ 60 h, X_{C2H6} = 27%, S_{C2H4} = 86%), demonstrating excellent stability (Figure S17). ICP analysis showed a small (0.03 wt%) decrease in boron content after ~20 h ODHE, which could result from boron oxide vaporization, but afterward, the boron content remained constant up to ~60 h ODHE, the longest time investigated (Table S1). The SEM images of the spent B-CHA catalyst showed nearly unchanged morphology after this period (Figure S6C). The micropore volume, however, decreased from 0.26 cm^3 g^{-1} to 0.24 cm^3 g^{-1} after ~20 h ODHE, and then to 0.20 cm^3 g^{-1} after ~60 h ODHE (Table S1).

Kinetic Investigation of ODHE over the B-CHA Catalyst. Experiments with different catalyst amounts were carried out first to rule out any mass and diffusion transfer limitations (Figure S18).[86] Since the ethane consumption rate ($-r_{C2H6}$) normalized by the catalyst mass of different catalyst amounts remained the same in all the measurements, we conclude that the reactor operated under a kinetics-controlled regime (i.e., there were no substantial mass transfer limitations). Moreover, this result also shows that the reactor operated under near isothermal conditions. A catalyst weight of 125 mg is used for further study to maintain differential reaction conditions in the reactor.[45]

The apparent activation energies (E_{app}) of ethane conversion are clearly different (317 and 125 kJ mol^{-1} over *h*-BN and B-CHA respectively, Figures 3A and S19). Our experimental E_{app} over *h*-BN matches the reported values (344 kJ mol^{-1} for fresh *h*-BN and 283 kJ mol^{-1} for activated *h*-BN).[21] The rate orders of $-r_{C2H6}$ on p_{C2H6} and p_{O2} were measured at three different temperatures (Figures 3B-D).[26,27,29,45] At 560 and 580 °C, $-r_{C2H6}$ over B-CHA showed nearly zero-order dependence on p_{O2} when p_{O2} was higher than 5.4 kPa, and first-order dependence on p_{C2H6}. At 600 °C, $-r_{C2H6}$ exhibited similar dependence on p_{O2}, and the ethane reaction order increased to 1.29.[30] Although ODHE over B-CHA showed Langmuir adsorption dependence on p_{O2} at all temperatures, the ethane reaction orders are unexpected because most boron-catalyzed ODHs have second-order dependence on the partial pressure of the alkane.[26–28] At 560 and 580 °C, the ethane reaction orders over B-CHA resembled the propane reaction order of ODHP over B-MFI as reported by Zhou et al.,[18] and that over the V_2O_5 supported on amorphous $AlPO_4$ as reported by Andersson.[87] First-order dependence may result from the microporous character of B-CHA, leading to differences in catalytic kinetics from non-porous *h*-BN.

In B-CHA, ethane activation is likely to occur inside the zeolite micropores. The ethane reaction order of 1 suggests the ethane activation on the surface, while the increased ethane

reaction order to 1.29 at 600 °C may indicate more activation in the gas phase at higher temperatures. This could also explain the sudden reactivity increase at 600 °C and is consistent with the high E_{app} of *h*-BN,[12,19,88] while E_{app} is usually higher when gas-phase radicals are involved in the mechanism and ethane activation happens mostly in the gas phase for *h*-BN catalyzed ODHE.

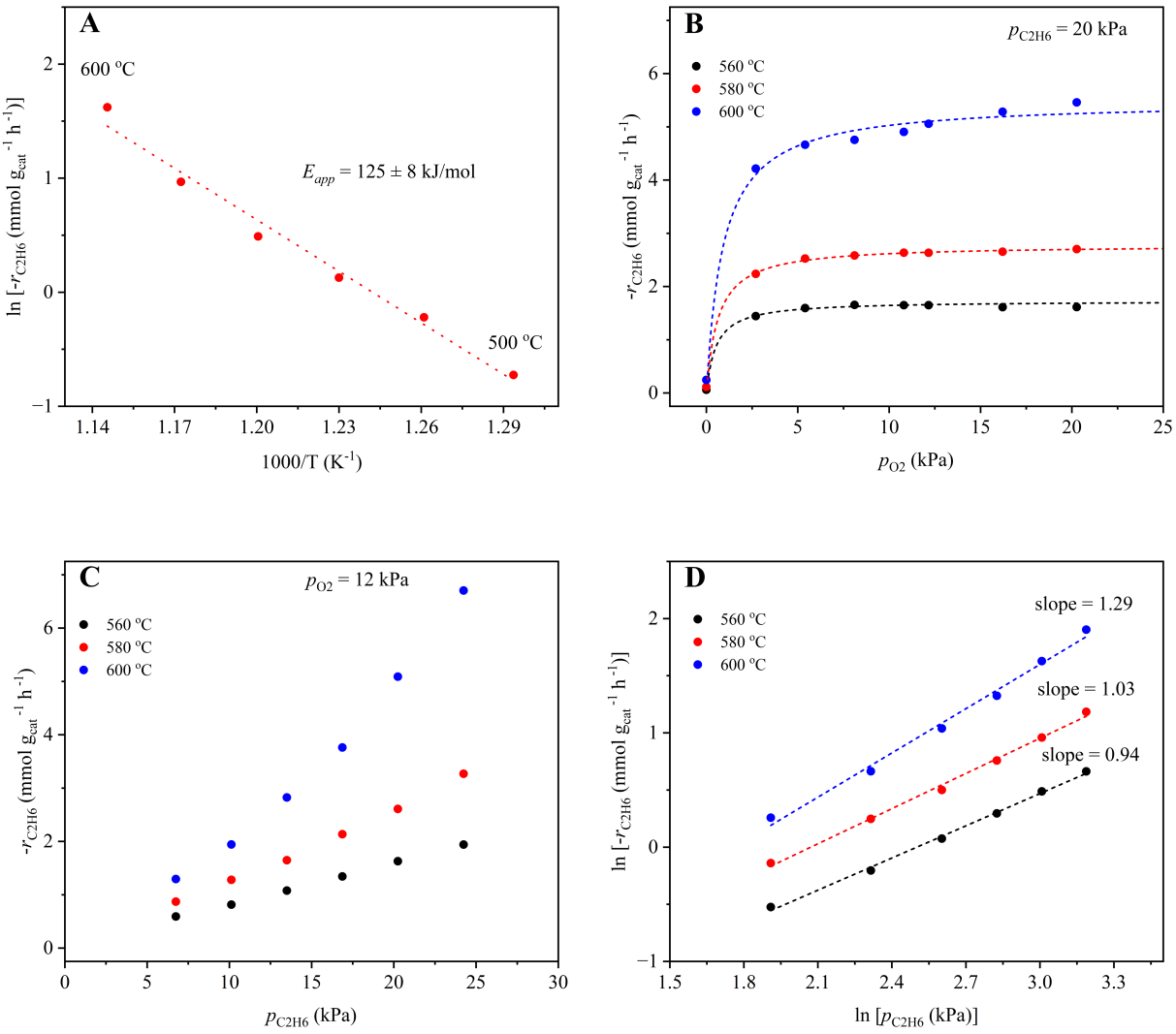

Figure 3. (**A**) The apparent activation energy (E_{app}) of ODHE over the B-CHA catalyst. The short-dashed line represents the linear fitting result. (**B**) Dependence of -r_{C2H6} on p_{O2} over the B-CHA catalyst. The short-dashed lines represent the simulated Langmuir adsorption isotherms. (**C**) Dependence of -r_{C2H6} on p_{C2H6} over the B-CHA catalyst. (**D**) Reaction orders of C_2H_6 of ODHE over the B-CHA catalyst. The short-dashed lines represent the linear fitting results.

High Concentration of Silanol Groups for B-CHA. The ^{29}Si MAS NMR spectra of B-CHA contain signals from -93 to -102 ppm and from -109 to -113 ppm that are assigned to Q^3 and Q^4 Si atoms.[89,90] The spectrum of the *as-made* B-CHA reveals that the framework of this sample is highly defective, with a $Q_3/(Q_3+Q_4)$ ratio of 0.44 (Figure S20A and Table S3), reflecting the presence of

a network of hydrogen-bonded siloxy groups balancing the positive charge of the structure-directing agent (SDA). The TGA trace of the as-made B-CHA shows there is one SDA per CHA cage (Figure S21A). Calcination in air to remove the organic SDA condensed many of these silanol groups, reducing the $Q_3/(Q_3+Q_4)$ ratio to 0.25 (Figure S20B). This number is still quite high, that is, the working catalyst can have 3-4 silanol groups per cage, an important consideration in view of their role as anchors of B sites. The amount of B in the sample is low and nominally dilute (Si/B~18), equivalent to a B concentration of 3.6 mmol $(cm^3)^{-1}$ in crystal volume. The high concentration of silanol groups of B-CHA leads to the even distribution on the surface area and sufficient exposure of boron species.

Active Boron Species. A solid-state NMR study of the fresh and spent B-CHA, including 1D ^{11}B MAS and 2D ^{11}B MQMAS NMR, was undertaken to investigate the structure and evolution of boron species in B-CHA (Figures 4 and 5).[18,26,91–99] As clearly shown in 2D ^{11}B MQMAS NMR (Figures 5A-D), at least three boron species are present in the fresh B-CHA, and the same boron species are found in the spent B-CHA, although the relative intensity changes after ODHE. This finding allows deconvolution of 1D ^{11}B MAS NMR spectra to produce the ^{11}B isotropic chemical shift δ_{iso} (ppm), quadrupolar coupling constant C_Q (MHz), asymmetry parameter (η), and the relative intensity (%) of the three major boron sites found in the corresponding 2D ^{11}B MQMAS. The fresh B-CHA has three observed boron species with δ_{iso} at -1.6, 14.0, and 16.3 ppm, and the spent B-CHA after ~20 and ~60 h ODHE also have three boron species with δ_{iso} at -1.8, 11.1 and 17.4 ppm and δ_{iso} at -1.6, 10.2 and 15.8 ppm (Tables S4 and S5).

The strong peak at -1.6 ppm in the fresh B-CHA and those at -1.8 and -1.6 ppm in the spent B-CHA are assigned to the tetracoordinated boron (B[4]), denoted as species A (Table 1).[18,93,95,97–99]

Species A may result from the reversible conversion of the trigonal boron (B[3]) that is anchored in the framework with three B-O-Si bonds.[92,95,99] The peak at 14.0 ppm in the fresh B-CHA and those at 11.1 and 10.2 ppm in the spent B-CHA could be assigned to $B(OSi)_2(OH)$ or $B(OSi)_2(OB)$, due to the down-field shift in observed δ_{iso} compared to the fully incorporated B in the chabazite framework.[26,92] However, considering that boron in the samples is so dilute (Si/B~18), that diffusion of $B(OH)_3$ through 8-ring windows is sterically constrained but required to form B-O-B linkages with B groups in other cages, and that the presence of trigonal extra-framework boron is not supported by 1D ^{11}B MAS NMR spectra, the presence of $B(OSi)_2(OB)$ moieties is ruled out and the peaks are thus assigned to $B(OSi)_2(OH)$, denoted as species B. The fact that C_Q of species B is much larger than that of species A (Table S5), indicating the high molecular symmetry observed in species A no longer exists in species B, supports this assignment. The weak peak at 16.3 ppm in the fresh B-CHA and those at 17.4 and 15.8 ppm in the spent B-CHA could be assigned to $B(OSi)(OH)_x(OB)_{2-x}$ (x = 1-2).[26,95] For the same reasons stated above, the presence of B-O-B linkages in the samples is highly unlikely and the signals are then assigned to $B(OSi)(OH)_2$, denoted as species C. Extra-framework boron (18~19 ppm), such as H_3BO_3, is absent in the spent catalyst, indicating negligible leaching of framework boron sites after ODHE.

The comparison of the relative intensities of each species across time shows that the relative intensities of species A and B decrease and that of species C increases after ~20 and ~60 h ODHE. The decrease of species A (51% to 40% after ~20 h ODHE and to 37% after ~60 h ODHE) results from the hydrolysis of framework B-O-Si groups by water produced under ODHE conditions,[92,95,99] causing the formation of $B(OSi)_2(OH)$ (species B), and further to $B(OSi)(OH)_2$ (species C). $B(OSi)(OH)_2$ is also suggested as the isolated active site in boron-catalyzed ODHP.[18] The monotonic increase of the relative intensity of species C is consistent with the increasing

reactivity over time (Figure 2D), suggesting that species C is responsible for initiating the ODHE activity in B-CHA. Also, the amount of species C is likely to reach a steady state as time-on-stream gets longer, and it was shown that steam treatments can shorten the time needed to reach the steady state.

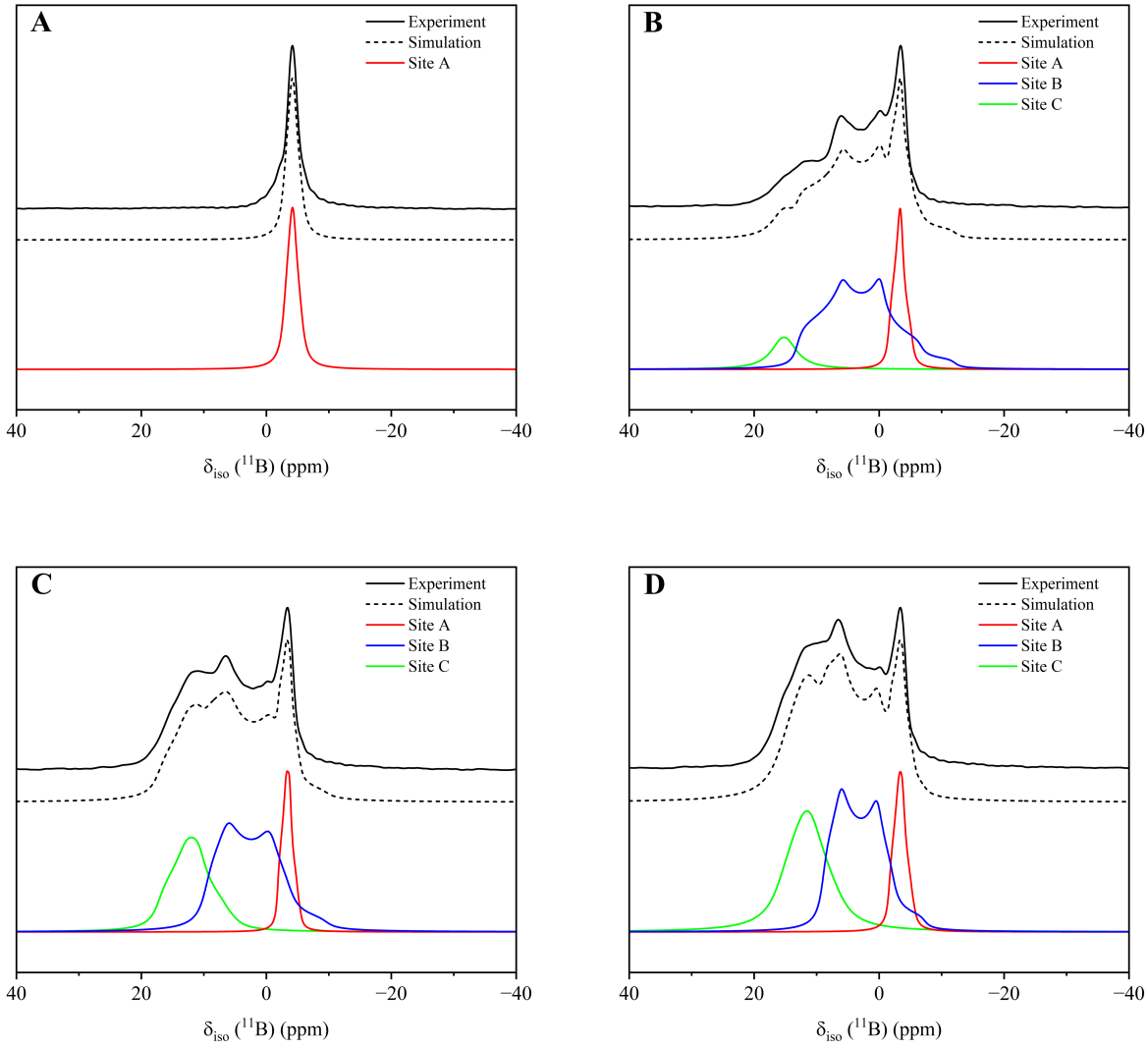

Figure 4. 1D ^{11}B MAS NMR spectra of (**A**) the as-made B-CHA, (**B**) the fresh B-CHA, (**C**) the spent B-CHA (20 h ODHE), and (**D**) the spent B-CHA (60 h ODHE) catalysts.

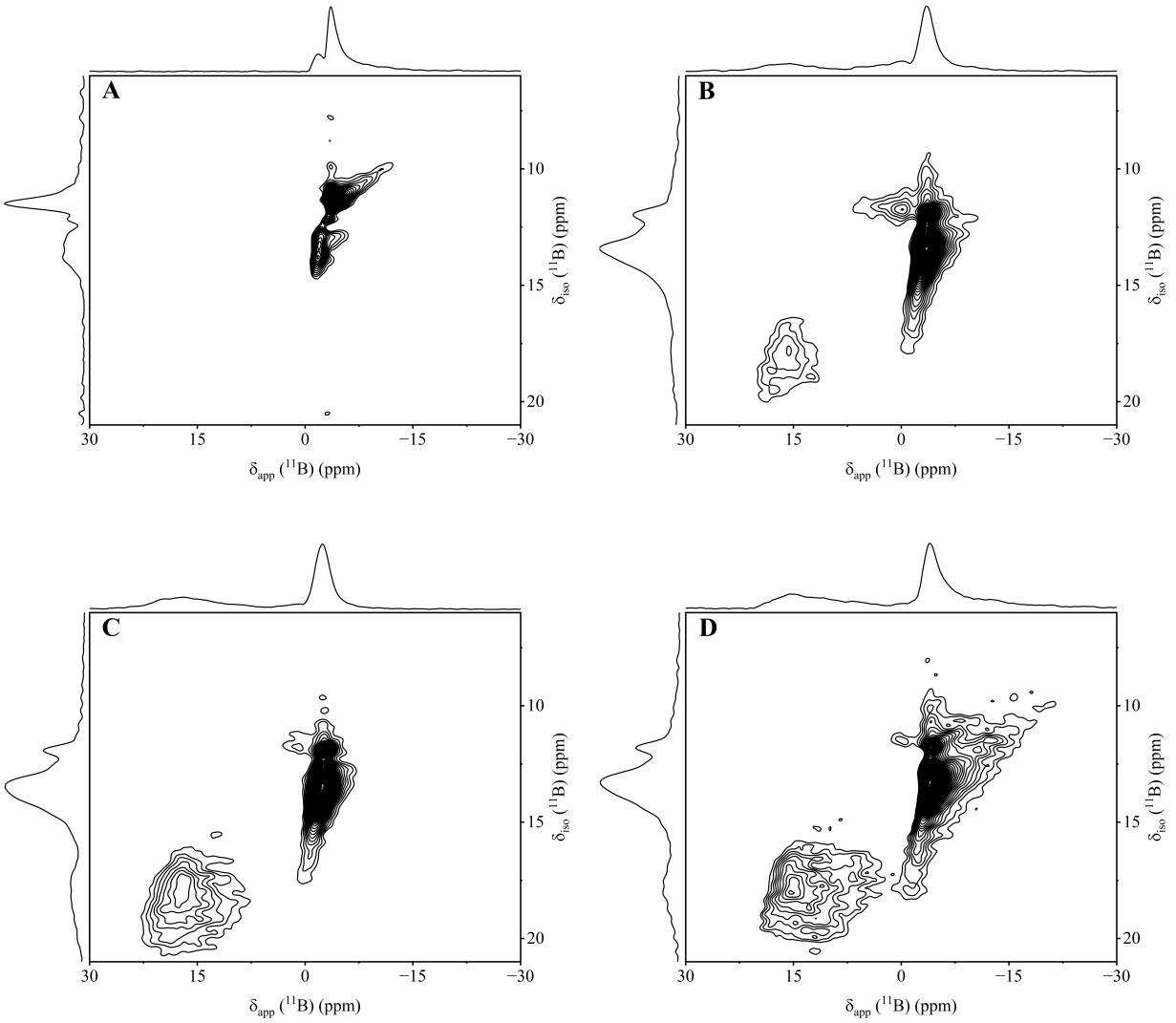

Figure 5. 2D ^{11}B MQMAS NMR spectra of (**A**) the as-made B-CHA, (**B**) the fresh B-CHA, (**C**) the spent B-CHA (20 h ODHE), and (**D**) the spent B-CHA (60 h ODHE) catalysts.

Table 1. Structure of the boron species in the fresh and spent B-CHA catalysts as determined from 1D ^{11}B MAS NMR spectra.

Site	A	B	C
Structure	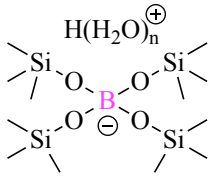	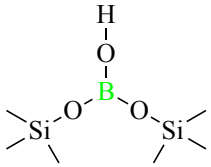	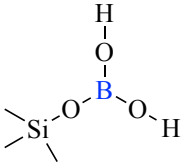

FTIR spectroscopy was also employed to understand the evolution of B-CHA in ODHE (Figure S22). A band at 1380 to 1400 cm^{-1}, representing the trigonal boron (B[3]),[18,99] grows as the temperature increases, possibly caused by the transformation of B[4] to B[3] through the sample dehydration, with the B-O bond being broken by the protonated oxygen. On the other hand, the band at 3740 to 3745 cm^{-1}, which characterizes the silanol groups (Si-OH),[100–102] decreases with increasing temperature, a result of the condensation of B-OH with Si-OH groups at high temperature. A broad peak from 3450 to 3680 cm^{-1}, which might result either from the H-bond interaction between B-OH and nearby Si-OH groups or from the presence of tetrahedral vacancies in the zeolite framework giving rise to H-bonded silanol groups that are more stable to dehydration, is present in the fresh and spent B-CHA.[94] The stronger peaks of B[3] (1380 to 1400 cm^{-1}) and B-OH (3450 to 3680 cm^{-1}) in the spent B-CHA are consistent with the transformation of species A (B[4]) to species B (B[3] with one B-OH bond) and further to species C (B[3] with two B-OH bond) under the ODHE conditions.

- **Conclusions**

We have shown that B-CHA zeolites catalyze the ODHE reaction at fast rates and with excellent selectivity and stability. The large micropore volume, high surface area and abundant OH groups in B-CHA contribute to the excellent performance of B-CHA. The kinetic study with ethane reaction orders from 1-1.29 is used to identify the transition of surface initiation to gas-phase initiation mechanism. Partially bonded-framework boron species $B(OSi)_2(OH)$ and $B(OSi)(OH)_2$ are identified as the active sites using NMR technique.

B-CHA is one amongst many small-, medium- and large-pore borosilicate zeolites that have been synthesized by the zeolite community, and there may be existing materials that display similar or better catalytic properties than B-CHA. Our results show that microporous environments can be engineered in ways that have not been explored and that could lead to other valuable routes to chemical production.

ASSOCIATED CONTENT

Supporting Information. The following files are available free of charge.

Structural characterizations, a summary of ODHE literature, product selectivity, activation energy, volumetric consumption rates, 1D ^{29}Si MAS NMR, 1D ^{11}B MAS NMR, FTIR spectra, and formation of carbon monoxide (PDF)

AUTHOR INFORMATION

Corresponding Author

*Raul F. Lobo: Center for Catalytic Science and Technology, Department of Chemical and Biomolecular Engineering, University of Delaware, Newark, Delaware 19716, United States; Email: lobo@udel.edu

Author Contributions

Mi Jen Kuo: Data curation, formal analysis, investigation, methodology, validation, visualization, writing, **Xinlei Huang:** investigation, **Sunkyu Kim:** investigation, **Nicholas Houck:** investigation, **Shi Bai:** NMR experiments, **Dionisios G. Vlachos:** mechanism conceptualization, and **Raul F. Lobo:** conceptualization, funding acquisition, methodology, project administration, resources, supervision, writing (review & editing).

Funding Sources

NSF CBET-1803246 and NSF-FMRG-2134471

ACKNOWLEDGMENT

This material is based upon work supported by the National Science Foundation under Grants Numbers: CBET-1803246 and FMRG-2134471.

REFERENCES

(1) *Production Capacity of Ethylene Worldwide from 2018 to 2021*; 2020. https://www.statista.com/statistics/1067372/global-ethylene-production-capacity/ (accessed 2023-06-03).

(2) Najari, S.; Saeidi, S.; Concepcion, P.; Dionysiou, D. D.; Bhargava, S. K.; Lee, A. F.; Wilson, K. Oxidative Dehydrogenation of Ethane: Catalytic and Mechanistic Aspects and Future Trends. *Chem. Soc. Rev.* **2021**, *50* (7), 4564–4605. https://doi.org/10.1039/D0CS01518K.

(3) *Ethene (Ethylene)*; The Essential Chemical Industry - online, 2017. https://www.essentialchemicalindustry.org/chemicals/ethene.html (accessed 2023-07-07).

(4) Sadrameli, S. M. Thermal/Catalytic Cracking of Hydrocarbons for the Production of Olefins: A State-of-the-Art Review I: Thermal Cracking Review. **2015**.

(5) *Technology Roadmap - Energy and GHG Reductions in the Chemical Industry via Catalytic Processes*; 2013. https://www.iea.org/reports/technology-roadmap-energy-and-ghg-reductions-in-the-chemical-industry-via-catalytic-processes (accessed 2023-06-03).

(6) Saito, H.; Sekine, Y. Catalytic Conversion of Ethane to Valuable Products through Non-Oxidative Dehydrogenation and Dehydroaromatization. *RSC Advances* **2020**, *10* (36), 21427–21453. https://doi.org/10.1039/d0ra03365k.

(7) Bruijnincx, P. C. A.; Weckhuysen, B. M. Shale Gas Revolution: An Opportunity for the Production of Biobased Chemicals? *Angew. Chem. Int. Ed.* **2013**.

(8) Zimmermann, H.; Walzl, R. Ethylene. In *Ullmann's Encyclopedia of Industrial Chemistry*; John Wiley & Sons, Ltd, 2009. https://doi.org/10.1002/14356007.a10_045.pub3.

(9) Ghanta, M.; Fahey, D.; Subramaniam, B. Environmental Impacts of Ethylene Production from Diverse Feedstocks and Energy Sources. **2014**.

(10) Gaffney, A. M. Ethylene Production via Oxidative Dehydrogenation of Ethane Using M1 Catalyst. *Catalysis Today* **2017**.

(11) Tian, J.; Li, J.; Qian, S.; Zhang, Z.; Wan, S.; Wang, S.; Lin, J.; Wang, Y. Understanding the Origin of Selective Oxidative Dehydrogenation of Propane on Boron-Based Catalysts. *Applied Catalysis A: General* **2021**, *623*. https://doi.org/10.1016/j.apcata.2021.118271.

(12) Lu, W. D.; Qiu, B.; Liu, Z. K.; Wu, F.; Lu, A. H. Supported Boron-Based Catalysts for Oxidative Dehydrogenation of Light Alkanes to Olefins. *Catalysis Science and Technology* **2023**. https://doi.org/10.1039/d2cy02098j.

(13) Morales, E.; Lunsford', A. H. *Oxidative Dehydrogenation of Ethane over a Lithium-Promoted Magnesium Oxide Catalyst*; 1989; Vol. 118, pp 255–281.

(14) Melzer, D.; Xu, P.; Hartmann, D.; Zhu, Y.; Browning, N. D.; Sanchez-Sanchez, M.; Lercher, J. A. Atomic-Scale Determination of Active Facets on the MoVTeNb Oxide M1 Phase and Their Intrinsic Catalytic Activity for Ethane Oxidative Dehydrogenation. *Angewandte Chemie International Edition* **2016**, *55* (31), 8873–8877.

(15) Arnold, S. C.; Gaffney, A. M.; Song, R.; Yeh, C. Y. Process for Producing Ethylene via Oxidative Dehydrogenation (ODH) of Ethane, 2013.

(16) Stefanie Nehlsen. *Clariant Unveils Groundbreaking Catalysts Developed Jointly with Linde Engineering for Novel Ethylene Production Technology*. https://www.clariant.com/en/Corporate/News/2021/10/Clariant-unveils-groundbreaking-catalysts-developed-jointly-with-Linde-Engineering-for-novel-ethylen (accessed 2023-08-31).

(17) Grant, J. T.; Carrero, C. A.; Goeltl, F.; Venegas, J.; Mueller, P.; Burt, S. P.; Specht, S. E.; McDermott, W. P.; Chieregato, A.; Hermans, I. Selective Oxidative Dehydrogenation of Propane to Propene Using Boron Nitride Catalysts. *Science* **2016**, *354* (6319), 1570–1573. https://doi.org/10.1126/science.aaf7885.
(18) Zhou, H.; Yi, X.; Hui, Y.; Wang, L.; Chen, W.; Qin, Y.; Wang, M.; Ma, J.; Chu, X.; Wang, Y.; Hong, X.; Chen, Z.; Meng, X.; Wang, H.; Zhu, Q.; Song, L.; Zheng, A.; Xiao, F.-S. *Isolated Boron in Zeolite for Oxidative Dehydrogenation of Propane*. https://www.science.org.
(19) Shi, L.; Wang, Y.; Yan, B.; Song, W.; Shao, D.; Lu, A. H. Progress in Selective Oxidative Dehydrogenation of Light Alkanes to Olefins Promoted by Boron Nitride Catalysts. *Chemical Communications* **2018**, *54* (78), 10936–10946. https://doi.org/10.1039/c8cc04604b.
(20) Shi, L.; Yan, B.; Shao, D.; Jiang, F.; Wang, D.; Lu, A.-H. Selective Oxidative Dehydrogenation of Ethane to Ethylene over a Hydroxylated Boron Nitride Catalyst. *Chinese Journal of Catalysis* **2017**, *38* (2), 389–395. https://doi.org/10.1016/S1872-2067(17)62786-4.
(21) Zhou, Y.; Lin, J.; Li, L.; Pan, X.; Sun, X.; Wang, X. Enhanced Performance of Boron Nitride Catalysts with Induction Period for the Oxidative Dehydrogenation of Ethane to Ethylene. *Journal of Catalysis* **2018**, *365*, 14–23. https://doi.org/10.1016/j.jcat.2018.05.023.
(22) Shi, L.; Wang, D.; Lu, A.-H. A Viewpoint on Catalytic Origin of Boron Nitride in Oxidative Dehydrogenation of Light Alkanes. *Chinese Journal of Catalysis* **2018**, *39* (5), 908–913. https://doi.org/10.1016/S1872-2067(18)63060-8.
(23) Huang, R.; Zhang, B.; Wang, J.; Wu, K. H.; Shi, W.; Zhang, Y.; Liu, Y.; Zheng, A.; Schlögl, R.; Su, D. S. Direct Insight into Ethane Oxidative Dehydrogenation over Boron Nitrides. *ChemCatChem* **2017**, *9* (17), 3293–3297. https://doi.org/10.1002/cctc.201700725.
(24) Xu, C.; Ge, C.; Sun, D.; Fan, Y.; Wang, X.-B. Boron Nitride Materials as Emerging Catalysts for Oxidative Dehydrogenation of Light Alkanes. *Nanotechnology* **2022**, *33* (43), 432003. https://doi.org/10.1088/1361-6528/ac7c23.
(25) Wu, Z.; Zhou, Y.; Ying, H.; Lin, J.; Han, W.-Q. Oxidative Dehydrogenation of Ethane Using Porous Hexagonal Boron Nitride Microtubes. *Chemical Physics Letters* **2020**, *746*, 137294. https://doi.org/10.1016/j.cplett.2020.137294.
(26) Gao, B.; Qiu, B.; Zheng, M.; Liu, Z.; Lu, W.-D.; Wang, Q.; Xu, J.; Deng, F.; Lu, A.-H. Dynamic Self-Dispersion of Aggregated Boron Clusters into Stable Oligomeric Boron Species on MFI Zeolite Nanosheets under Oxidative Dehydrogenation of Propane. *ACS Catalysis* **2022**, *12* (12), 7368–7376. https://doi.org/10.1021/acscatal.2c01622.
(27) Tian, H.; Xu, B. Oxidative Co-Dehydrogenation of Ethane and Propane over h-BN as an Effective Means for C–H Bond Activation and Mechanistic Investigations. *Chinese Journal of Catalysis* **2022**, *43* (8), 2173–2182. https://doi.org/10.1016/S1872-2067(21)64042-1.
(28) Venegas, J. M.; Zhang, Z.; Agbi, T. O.; McDermott, W. P.; Alexandrova, A.; Hermans, I. Why Boron Nitride Is Such a Selective Catalyst for the Oxidative Dehydrogenation of Propane. *Angewandte Chemie - International Edition* **2020**, *59* (38), 16527–16535. https://doi.org/10.1002/anie.202003695.

(29) Shi, L.; Wang, D.; Song, W.; Shao, D.; Zhang, W. P.; Lu, A. H. Edge-Hydroxylated Boron Nitride for Oxidative Dehydrogenation of Propane to Propylene. *ChemCatChem* **2017**, *9* (10), 1788–1793. https://doi.org/10.1002/cctc.201700004.
(30) Tian, H.; Liu, Y.; Xu, B. Kinetic Investigations of Oxidative Dehydrogenation of Propane on Boron Oxide in Confined Spaces. *Catalysis Today* **2023**, 114048. https://doi.org/10.1016/j.cattod.2023.114048.
(31) Grabowski, R. Kinetics of Oxidative Dehydrogenation of C_2 -C_3 Alkanes on Oxide Catalysts. *Catalysis Reviews* **2006**, *48* (2), 199–268. https://doi.org/10.1080/01614940600631413.
(32) Xu, S.; Zheng, A.; Wei, Y.; Chen, J.; Li, J.; Chu, Y.; Zhang, M.; Wang, Q.; Zhou, Y.; Wang, J.; Deng, F.; Liu, Z. Direct Observation of Cyclic Carbenium Ions and Their Role in the Catalytic Cycle of the Methanol-to-Olefin Reaction over Chabazite Zeolites. *Angew. Chem. Int. Ed.* **2013**, *52* (44), 11564–11568. https://doi.org/10.1002/anie.201303586.
(33) Wang, J.; Zhao, H.; Haller, G.; Li, Y. Recent Advances in the Selective Catalytic Reduction of NOx with NH3 on Cu-Chabazite Catalysts. *Applied Catalysis B: Environmental* **2017**, *202*, 346–354. https://doi.org/10.1016/j.apcatb.2016.09.024.
(34) Olson, D. H.; Camblor, M. A.; Villaescusa, L. A.; Kuehl, G. H. Light Hydrocarbon Sorption Properties of Pure Silica Si-CHA and ITQ-3 and High Silica ZSM-58. *Microporous and Mesoporous Materials* **2004**, *67* (1), 27–33. https://doi.org/10.1016/j.micromeso.2003.09.025.
(35) Qiu, B.; Lu, W. D.; Gao, X. Q.; Sheng, J.; Yan, B.; Ji, M.; Lu, A. H. Borosilicate Zeolite Enriched in Defect Boron Sites Boosting the Low-Temperature Oxidative Dehydrogenation of Propane. *Journal of Catalysis* **2022**, *408*, 133–141. https://doi.org/10.1016/j.jcat.2022.02.017.
(36) Regli, L.; Bordiga, S.; Lamberti, C.; Lillerud, K. P.; Zones, S. I.; Zecchina, A. Effect of Boron Substitution in Chabazite Framework: IR Studies on the Acidity Properties and Reactivity towards Methanol. *Journal of Physical Chemistry C* **2007**, *111* (7), 2992–2999. https://doi.org/10.1021/jp064048w.
(37) Loiland, J. A.; Lobo, R. F. Low Temperature Catalytic NO Oxidation over Microporous Materials. *Journal of Catalysis* **2014**, *311*, 412–423. https://doi.org/10.1016/j.jcat.2013.12.013.
(38) Pham, T. D.; Xiong, R.; Sandler, S. I.; Lobo, R. F. Experimental and Computational Studies on the Adsorption of CO2 and N2 on Pure Silica Zeolites. *Microporous and Mesoporous Materials* **2014**, *185*, 157–166. https://doi.org/10.1016/j.micromeso.2013.10.030.
(39) Yuan, Y.; Lobo, R. F. Propane Dehydrogenation over Extra-Framework In(i) in Chabazite Zeolites. *Chemical Science* **2022**, *13* (10), 2954–2964. https://doi.org/10.1039/d1sc05866e.
(40) Cho, H. J.; Kuo, M. J.; Ye, M.; Kurz, Y.; Yuan, Y.; Lobo, R. F. Selective Synthesis of 4,4′-Dimethylbiphenyl from 2-Methylfuran. *ACS Sustainable Chemistry and Engineering* **2021**, No. Ii. https://doi.org/10.1021/acssuschemeng.0c09227.
(41) Cory, D. G.; Ritchey, W. M. Suppression of Signals from the Probe in Bloch Decay Spectra. *Journal of Magnetic Resonance (1969)* **1988**, *80* (1), 128–132. https://doi.org/10.1016/0022-2364(88)90064-9.
(42) Massiot, D.; Touzo, B.; Trumeau, D.; Coutures, J. P.; Virlet, J.; Florian, P.; Grandinetti, P. J. Two-Dimensional Magic-Angle Spinning Isotropic Reconstruction Sequences for

Quadrupolar Nuclei. *Solid State Nuclear Magnetic Resonance* **1996**, *6* (1), 73–83. https://doi.org/10.1016/0926-2040(95)01210-9.
(43) Hayashi, S.; Hayamizu, K. Shift References in High-Resolution Solid-State NMR. *BCSJ* **1989**, *62* (7), 2429–2430. https://doi.org/10.1246/bcsj.62.2429.
(44) Love, A. M.; Cendejas, M. C.; Thomas, B.; McDermott, W. P.; Uchupalanun, P.; Kruszynski, C.; Burt, S. P.; Agbi, T.; Rossini, A. J.; Hermans, I. Synthesis and Characterization of Silica-Supported Boron Oxide Catalysts for the Oxidative Dehydrogenation of Propane. *Journal of Physical Chemistry C* **2019**, *123* (44), 27000–27011. https://doi.org/10.1021/acs.jpcc.9b07429.
(45) Heracleous, E.; Lemonidou, A. A. Ni-Nb-O Mixed Oxides as Highly Active and Selective Catalysts for Ethene Production via Ethane Oxidative Dehydrogenation. Part II: Mechanistic Aspects and Kinetic Modeling. *Journal of Catalysis* **2006**, *237* (1), 175–189. https://doi.org/10.1016/j.jcat.2005.11.003.
(46) Wang, Y.; Chen, J.; Lei, X.; Ren, Y.; Wu, J. Preparation of High Silica Microporous Zeolite SSZ-13 Using Solid Waste Silica Fume as Silica Source. *Advanced Powder Technology* **2018**, *29* (5), 1112–1118. https://doi.org/10.1016/j.apt.2018.02.001.
(47) Botella, P.; López Nieto, J. M.; Dejoz, A.; Vázquez, M. I.; Martínez-Arias, A. Mo–V–Nb Mixed Oxides as Catalysts in the Selective Oxidation of Ethane. *Catalysis Today* **2003**, *78* (1–4), 507–512. https://doi.org/10.1016/S0920-5861(02)00338-3.
(48) Chao, Z.-S. [No Title Found]. *Catalysis Letters* **2003**, *88* (3/4), 147–154. https://doi.org/10.1023/A:1024082310691.
(49) Lisi, L.; Ruoppolo, G.; Casaletto, M. P.; Galli, P.; Massucci, M. A.; Patrono, P.; Pinzari, F. Vanadium-Metal(IV)Phosphates as Catalysts for the Oxidative Dehydrogenation of Ethane. *Journal of Molecular Catalysis A: Chemical* **2005**, *232* (1–2), 127–134. https://doi.org/10.1016/j.molcata.2005.01.035.
(50) López, E.; Heracleous, E.; Lemonidou, A. A.; Borio, D. O. Study of a Multitubular Fixed-Bed Reactor for Ethylene Production via Ethane Oxidative Dehydrogenation. *Chemical Engineering Journal* **2008**, *145* (2), 308–315. https://doi.org/10.1016/j.cej.2008.08.029.
(51) Li, J.; Li, R.; Wang, C.; Huang, C.; Weng, W.; Wan, H. Oxidative Dehydrogenation of Ethane to Ethylene over Mesoporous Ni-Based Catalysts. *Chinese Journal of Catalysis* **2009**, *30* (8), 714–716. https://doi.org/10.1016/S1872-2067(08)60122-9.
(52) Smoláková, L.; Čapek, L.; Botková, Š.; Kovanda, F.; Bulánek, R.; Pouzar, M. Activity of the Ni–Al Mixed Oxides Prepared from Hydrotalcite-Like Precursors in the Oxidative Dehydrogenation of Ethane and Propane. *Top Catal* **2011**, *54* (16–18), 1151–1162. https://doi.org/10.1007/s11244-011-9737-3.
(53) Sanchis, R.; Delgado, D.; Agouram, S.; Soriano, M. D.; Vázquez, M. I.; Rodríguez-Castellón, E.; Solsona, B.; Nieto, J. M. L. NiO Diluted in High Surface Area TiO 2 as an Efficient Catalyst for the Oxidative Dehydrogenation of Ethane. *Applied Catalysis A: General* **2017**, *536*, 18–26. https://doi.org/10.1016/j.apcata.2017.02.012.
(54) Bulánek, R.; Novoveská, K.; Wichterlová, B. Oxidative Dehydrogenation and Ammoxidation of Ethane and Propane over Pentasil Ring Co-Zeolites. *Applied Catalysis A: General* **2002**, *235* (1–2), 181–191. https://doi.org/10.1016/S0926-860X(02)00263-6.
(55) Zhao, Y. B.; Tan, W. W.; Li, H.; Jia, X. H.; Wan, H. L. Oxidative Dehydrogenation of Ethane to Ethene over a Superbase Supported LiCl System. *Chinese Chemical Letters* **2010**, *21* (11), 1366–1369. https://doi.org/10.1016/j.cclet.2010.06.025.

(56) Lin, X.; Poeppelmeier, K. R.; Weitz, E. Oxidative Dehydrogenation of Ethane with Oxygen Catalyzed by K–Y Zeolite Supported First-Row Transition Metals. *Applied Catalysis A: General* **2010**, *381* (1–2), 114–120. https://doi.org/10.1016/j.apcata.2010.03.049.
(57) Kong, L.; Li, J.; Liu, Q.; Zhao, Z.; Sun, Q.; Liu, J.; Wei, Y. Promoted Catalytic Performances of Highly Dispersed V-Doped SBA-16 Catalysts for Oxidative Dehydrogenation of Ethane to Ethylene. *Journal of Energy Chemistry* **2016**, *25* (4), 577–586. https://doi.org/10.1016/j.jechem.2016.04.004.
(58) Ayari, F.; Charrad, R.; Asedegbega–Nieto, E.; Mhamdi, M.; Delahay, G.; Farhat, F.; Ghorbel, A. Ethane Oxidative Dehydrogenation over Ternary and Binary Mixtures of Alkaline and Alkaline Earth Chlorides Supported on Zeolites. *Microporous and Mesoporous Materials* **2017**, *250*, 65–71. https://doi.org/10.1016/j.micromeso.2017.05.010.
(59) Solsona, B.; López Nieto, J. M.; Concepción, P.; Dejoz, A.; Ivars, F.; Vázquez, M. I. Oxidative Dehydrogenation of Ethane over Ni–W–O Mixed Metal Oxide Catalysts. *Journal of Catalysis* **2011**, *280* (1), 28–39. https://doi.org/10.1016/j.jcat.2011.02.010.
(60) Silberova, B.; Fathi, M.; Holmen, A. Oxidative Dehydrogenation of Ethane and Propane at Short Contact Time. *Applied Catalysis A: General* **2004**, *276* (1–2), 17–28. https://doi.org/10.1016/j.apcata.2003.10.044.
(61) Adesina, A. A.; Cant, N. W.; Saberi-Moghaddam, A.; Szeto, C. H. L.; Trimm, D. L. Structural Effects in Oxidative Dehydrogenation of Hydrocarbons over a Vanadia-Molybdena-Niobia Catalyst. *J. Chem. Technol. Biotechnol.* **1998**, *72* (1), 19–22. https://doi.org/10.1002/(SICI)1097-4660(199805)72:1<19::AID-JCTB866>3.0.CO;2-N.
(62) Botella, P. Selective Oxidative Dehydrogenation of Ethane on MoVTeNbO Mixed Metal Oxide Catalysts. *Journal of Catalysis* **2004**, *225* (2), 428–438. https://doi.org/10.1016/j.jcat.2004.04.024.
(63) Conway, S. J.; Wang, D. J.; Lunsford, J. H. Selective Oxidation of Methane and Ethane over Li+-MgO-Cl− Catalysts Promoted with Metal Oxides. *Applied Catalysis A: General* **1991**, *79* (1), L1–L5. https://doi.org/10.1016/0926-860X(91)85001-E.
(64) Le Bars, J.; Auroux, A.; Forissier, M.; Vedrine, J. C. Active Sites of V2O5/γ-Al2O3Catalysts in the Oxidative Dehydrogenation of Ethane. *Journal of Catalysis* **1996**, *162* (2), 250–259. https://doi.org/10.1006/jcat.1996.0282.
(65) Brik, Y.; Kacimi, M.; Ziyad, M.; Bozon-Verduraz, F. Titania-Supported Cobalt and Cobalt–Phosphorus Catalysts: Characterization and Performances in Ethane Oxidative Dehydrogenation. *Journal of Catalysis* **2001**, *202* (1), 118–128. https://doi.org/10.1006/jcat.2001.3262.
(66) Luo, J. Z.; Zhou, X. P.; Chao, Z. S.; Wan, H. L. Oxidative Dehydrogenation of Ethane over BaF2 Promoted SmO3LaF3 Catalysts. *Applied Catalysis A: General* **1997**, *159* (1–2), 9–19. https://doi.org/10.1016/S0926-860X(97)00046-X.
(67) Au, C. T.; Chen, K. D.; Dai, H. X.; Liu, Y. W.; Ng, C. F. The Modification of Ho2O3 with BaCl2 for the Oxidative Dehydrogenation of Ethane. *Applied Catalysis A: General* **1999**, *177* (2), 185–191. https://doi.org/10.1016/S0926-860X(98)00267-1.
(68) Zhang, X.; Ye, Q.; Xu, B.; He, D. Oxidative Dehydrogenation of Ethane over Co–BaCO3 Catalysts Using CO2 as Oxidant: Effects of Co Promoter. *Catal Lett* **2007**, *117* (3–4), 140–145. https://doi.org/10.1007/s10562-007-9122-9.

(69) Mulla, S. A Comparative Study on Non-Catalytic and Catalytic Oxidative Dehydrogenation of Ethane to Ethylene. *Applied Catalysis A: General* **2002**, *226* (1–2), 73–78. https://doi.org/10.1016/S0926-860X(01)00884-5.
(70) Wang, D. J.; Rosynek, M. P.; Lunsford, J. H. The Effect of Chloride Ions on a Li+-MgO Catalyst for the Oxidative Dehydrogenation of Ethane. *Journal of Catalysis* **1995**, *151* (1), 155–167. https://doi.org/10.1006/jcat.1995.1018.
(71) Tope, B.; Zhu, Y.; Lercher, J. A. Oxidative Dehydrogenation of Ethane over Dy2O3/MgO Supported LiCl Containing Eutectic Chloride Catalysts. *Catalysis Today* **2007**, *123* (1–4), 113–121. https://doi.org/10.1016/j.cattod.2007.02.020.
(72) Kumar, C. P.; Gaab, S.; Müller, T. E.; Lercher, J. A. Oxidative Dehydrogenation of Light Alkanes on Supported Molten Alkali Metal Chloride Catalysts. *Top Catal* **2008**, *50* (1–4), 156–167. https://doi.org/10.1007/s11244-008-9102-3.
(73) Choudhary, V. R.; Mulla, S. A. R.; Rane, V. H. Oxidative Coupling of Methane and Oxidative Dehydrogenation of Ethane over Strontium-Promoted Rare Earth Oxide Catalysts. *J. Chem. Technol. Biotechnol.* **1998**, *71* (2), 167–172. https://doi.org/10.1002/(SICI)1097-4660(199802)71:2<167::AID-JCTB789>3.0.CO;2-F.
(74) Chen, X.; Yang, Q.; Chu, B.; An, H.; Cheng, Y. Valence Variation of Phase-Pure M1 MoVNbTe Oxide by Plasma Treatment for Improved Catalytic Performance in Oxidative Dehydrogenation of Ethane. *RSC Adv.* **2015**, *5* (111), 91295–91301. https://doi.org/10.1039/C5RA16517B.
(75) Blasco, T.; Nieto, J. M. L. Oxidative Dyhydrogenation of Short Chain Alkanes on Supported Vanadium Oxide Catalysts. *Applied Catalysis A: General* **1997**, *157* (1–2), 117–142. https://doi.org/10.1016/S0926-860X(97)00029-X.
(76) Heracleous, E.; Lemonidou, A. A. Ni-Nb-O Mixed Oxides as Highly Active and Selective Catalysts for Ethene Production via Ethane Oxidative Dehydrogenation. Part I: Characterization and Catalytic Performance. *Journal of Catalysis* **2006**, *237* (1), 162–174. https://doi.org/10.1016/j.jcat.2005.11.002.
(77) Botella, P.; Dejoz, A.; Lopeznieto, J.; Concepcion, P.; Vazquez, M. Selective Oxidative Dehydrogenation of Ethane over MoVSbO Mixed Oxide Catalysts. *Applied Catalysis A: General* **2006**, *298*, 16–23. https://doi.org/10.1016/j.apcata.2005.09.018.
(78) Ciambelli, P.; Galli, P.; Lisi, L.; Massucci, M. A.; Patrono, P.; Pirone, R.; Ruoppolo, G.; Russo, G. TiO2 Supported Vanadyl Phosphate as Catalyst for Oxidative Dehydrogenation of Ethane to Ethylene. *Applied Catalysis A: General* **2000**, *203* (1), 133–142. https://doi.org/10.1016/S0926-860X(00)00481-6.
(79) Liu, C.; Ozkan, U. S. Effect of Chlorine on Redox and Adsorption Characteristics of Mo/Si:Ti Catalysts in the Oxidative Dehydrogenation of Ethane. *Journal of Molecular Catalysis A: Chemical* **2004**, *220* (1), 53–65. https://doi.org/10.1016/j.molcata.2004.03.049.
(80) Concepción, P.; Corma, A.; López Nieto, J. M.; Pérez-Pariente, J. Selective Oxidation of Hydrocarbons on V- and/or Co-Containing Aluminophosphate (MeAPO-5) Using Molecular Oxygen. *Applied Catalysis A: General* **1996**, *143* (1), 17–28. https://doi.org/10.1016/0926-860X(96)00068-3.
(81) Concepci n, P.; L pez Nieto, J. M.; P rez-Pariente, J. Oxidative Dehydrogenation of Ethane on a Magnesium-Vanadium Aluminophosphate (MgVAPO-5) Catalyst. *Catal Lett* **1994**, *28* (1), 9–15. https://doi.org/10.1007/BF00812464.

(82) Galli, A.; López Nieto, J. M.; Dejoz, A.; Vazquez, M. I. The Effect of Potassium on the Selective Oxidation Ofn-Butane and Ethane over Al2O3-Supported Vanadia Catalysts. *Catal Lett* **1995**, *34* (1–2), 51–58. https://doi.org/10.1007/BF00808321.
(83) Dai, H. X.; Ng, C. F.; Au, C. T. Raman Spectroscopic and EPR Investigations of Oxygen Species on SrCl2-Promoted Ln2O3 (Ln=Sm and Nd) Catalysts for Ethane-Selective Oxidation to Ethene. *Applied Catalysis A: General* **2000**, *202* (1), 1–15. https://doi.org/10.1016/S0926-860X(00)00453-1.
(84) Au, C. T.; Zhou, X. P.; Wan, H. L. The Activation of O2 and the Oxidative Dehydrogenation of C2H6 over SmOF Catalyst. *Catal Lett* **1996**, *40* (1–2), 101–104. https://doi.org/10.1007/BF00807464.
(85) Bodke, A. S.; Olschki, D. A.; Schmidt, L. D.; Ranzi, E. High Selectivities to Ethylene by Partial Oxidation of Ethane. *Science* **1999**, *285* (5428), 712–715. https://doi.org/10.1126/science.285.5428.712.
(86) Venegas, J. M.; Hermans, I. The Influence of Reactor Parameters on the Boron Nitride-Catalyzed Oxidative Dehydrogenation of Propane. *Organic Process Research and Development* **2018**, *22* (12), 1644–1652. https://doi.org/10.1021/acs.oprd.8b00301.
(87) Andersson, S. L. T. Kinetic Study of the Oxidative Dehydrogenation of Propane over Vanadia Supported on Amorphous AlPO4. *Applied Catalysis A: General* **1994**, *112* (2), 209–218. https://doi.org/10.1016/0926-860X(94)80220-3.
(88) Venegas, J. M.; McDermott, W. P.; Hermans, I. Serendipity in Catalysis Research: Boron-Based Materials for Alkane Oxidative Dehydrogenation. *Accounts of Chemical Research* **2018**, *51* (10), 2556–2564. https://doi.org/10.1021/acs.accounts.8b00330.
(89) Dellarocca, V.; Peña, M. L.; Rey, F.; Corma, A.; Coluccia, S.; Marchese, L. 29-P-30-Ti-MCM-48 with Different Titanium Loading: Synthesis, Spectroscopic Characterization and Catalytic Activity. In *Studies in Surface Science and Catalysis*; Elsevier, 2001; Vol. 135, p 319. https://doi.org/10.1016/S0167-2991(01)81725-0.
(90) Bal'zhinimaev, B. S.; Paukshtis, E. A.; Lapina, O. B.; Suknev, A. P.; Kirillov, V. L.; Mikenin, P. E.; Zagoriuko, A. N. Glass Fiber Materials as a New Generation of Structured Catalysts. In *Studies in Surface Science and Catalysis*; Elsevier, 2010; Vol. 175, pp 43–50. https://doi.org/10.1016/S0167-2991(10)75006-0.
(91) Love, A. M.; Thomas, B.; Specht, S. E.; Hanrahan, M. P.; Venegas, J. M.; Burt, S. P.; Grant, J. T.; Cendejas, M. C.; McDermott, W. P.; Rossini, A. J.; Hermans, I. Probing the Transformation of Boron Nitride Catalysts under Oxidative Dehydrogenation Conditions. *Journal of the American Chemical Society* **2019**, *141* (1), 182–190. https://doi.org/10.1021/jacs.8b08165.
(92) Hwang, S. J.; Chen, C. Y.; Zones, S. I. Boron Sites in Borosilicate Zeolites at Various Stages of Hydration Studied by Solid State NMR Spectroscopy. *Journal of Physical Chemistry B* **2004**, *108* (48), 18535–18546. https://doi.org/10.1021/jp0476904.
(93) Fild, C.; Shantz, D. F.; Lobo, R. F.; Koller, H. Cation-Induced Transformation of Boron-Coordination in Zeolites. *Physical Chemistry Chemical Physics* **2000**, *2* (13), 3091–3098. https://doi.org/10.1039/b002134m.
(94) Koller, H.; Chen, C.-Y.; Zones, S. I. Selectivities in Post-Synthetic Modification of Borosilicate Zeolites. *Top Catal* **2015**, *58* (7–9), 451–479. https://doi.org/10.1007/s11244-015-0382-0.

(95) Koller, H.; Fild, C.; Lobo, R. F. Variable Anchoring of Boron in Zeolite Beta. *Microporous and Mesoporous Materials* **2005**, *79* (1–3), 215–224. https://doi.org/10.1016/j.micromeso.2004.10.035.
(96) Regli, L.; Bordiga, S.; Busco, C.; Prestipino, C.; Ugliengo, P.; Zecchina, A.; Lamberti, C. Functionalization of Zeolitic Cavities: Grafting NH2 Groups in Framework T Sites of B-SSZ-13 - A Way to Obtain Basic Solids Catalysts? *Journal of the American Chemical Society* **2007**, *129* (40), 12131–12140. https://doi.org/10.1021/ja0721770.
(97) Kroeker, S.; Stebbins, J. F. Three-Coordinated Boron-11 Chemical Shifts in Borates. *Inorganic Chemistry* **2001**, *40* (24), 6239–6246. https://doi.org/10.1021/ic010305u.
(98) Fild, C.; Eckert, H.; Koller, H. Evidence for Selective Association of Tetrahedral BO4 Units with Na+ and of Trigonal BO3 Units with H+ in Dehydrated Zeolite B-ZSM-5 from Solid-State NMR Spectroscopy. *Angewandte Chemie - International Edition* **1998**, *37* (18), 2505–2507. https://doi.org/10.1002/(SICI)1521-3773(19981002)37:18<2505::AID-ANIE2505>3.0.CO;2-F.
(99) Millini, R.; Perego, G.; Bellussi, G. *Synthesis and Characterization of Boron-Containing Molecular Sieves*; 1999; Vol. 9, pp 13–34.
(100) Hadjiivanov, K. Identification and Characterization of Surface Hydroxyl Groups by Infrared Spectroscopy. In *Advances in Catalysis*; Elsevier, 2014; Vol. 57, pp 99–318. https://doi.org/10.1016/B978-0-12-800127-1.00002-3.
(101) Datka, J.; Piwowarska, Z. OH Groups in Boralites. *J. Chem. Soc., Faraday Trans. 1* **1989**, *85* (4), 837. https://doi.org/10.1039/f19898500837.
(102) Chu, C. T. W.; Chang, C. D. Isomorphous Substitution in Zeolite Frameworks. 1. Acidity of Surface Hydroxyls in [B]-, [Fe]-, [Ga]-, and [Al]-ZSM-5. *J. Phys. Chem.* **1985**, *89* (9), 1569–1571. https://doi.org/10.1021/j100255a005.

Table of Contents graphic